nanomaterials

MDPI

Article

Fabrication of Bi_2MoO_6 Nanosheets/TiO_2 Nanorod Arrays Heterostructures for Enhanced Photocatalytic Performance under Visible-Light Irradiation

Di Zhou [1], Rui Du [1], Zhenglong Hu [2,*], Shu Gao [1], Yafang Tu [1], Yunfei Fu [1], Guang Zheng [1,*] and Youhua Zhou [1]

[1] School of Optoelectronic Materials and Technologies, Jianghan University, Wuhan 430056, China; dizhou@jhun.edu.cn (D.Z.); durui199602@163.com (R.D.); milton_gao@jhun.edu.cn (S.G.); yafangtu@163.com (Y.T.); yffu89@jhun.edu.cn (Y.F.); xinge@whut.edu.cn (Y.Z.)
[2] Laboratory of Low-Dimension Functional Nanostructures and Devices, Hubei University of Science and Technology, Xianning 437100, China
* Correspondence: huzhenglong@hbust.edu.cn (Z.H.); mzheng88@foxmail.com (G.Z.)

Abstract: Bi_2MoO_6/TiO_2 heterostructures (HSs) were synthesized in the present study by growing Bi_2MoO_6 nanosheets on vertically aligned TiO_2 nanorod arrays using a two-step solvothermal method. Their morphology and structure were characterized by scanning electron microscopy (SEM) and X-ray diffraction (XRD), respectively. Excellent visible-light absorption was observed by UV–Vis absorption spectroscopy, which was attributed to the presence of the Bi_2MoO_6 nanosheets with a narrow-band-gap. The specific surface area and pore volume of the photocatalysts were significantly increased due to the hierarchical structure composed of Bi_2MoO_6 nanosheets and TiO_2 nanorods. The photoluminescence and photoelectrochemical characterizations showed improved separation and collection efficiency of the Bi_2MoO_6/TiO_2 HSs towards the interface charge carrier. The photocatalytic analysis of the Bi_2MoO_6/TiO_2 HSs demonstrated a significantly better methylene blue (MB) degradation efficiency of 95% within 3 h than pristine TiO_2 nanorod arrays under visible-light irradiation. After three photocatalytic cycles, the degradation rate remained at ~90%. The improved performance of the Bi_2MoO_6/TiO_2 HSs was attributed to the synergy among the extended absorption of visible light; the large, specific surface area of the hierarchical structure; and the enhanced separation efficiency of the photogenerated electron-hole pairs. Finally, we also established the Bi_2MoO_6/TiO_2 HSs band structure and described the photocatalytic dye degradation mechanism. The related electrochemical analysis and free-radical trapping experiments indicated that h^+, $\cdot O_2^-$ and ·OH have significant effects on the degradation process.

Keywords: Bi_2MoO_6; TiO_2 nanorod arrays; heterostructure; photodegradation; solvothermal method

Citation: Zhou, D.; Du, R.; Hu, Z.; Gao, S.; Tu, Y.; Fu, Y.; Zheng, G.; Zhou, Y. Fabrication of Bi_2MoO_6 Nanosheets/TiO_2 Nanorod Arrays Heterostructures for Enhanced Photocatalytic Performance under Visible-Light Irradiation. *Nanomaterials* **2022**, *12*, 574. https://doi.org/10.3390/nano12030574

Academic Editors: Vasco Teixeira and Vincenzo Vaiano

Received: 5 January 2022
Accepted: 29 January 2022
Published: 8 February 2022

1. Introduction

Light- and catalysis-assisted removal of pollutants and water electrolysis are popular processes because of their environmental friendliness. Titanium dioxide (TiO_2) is a popular photocatalyst because of its favorable electron mobility, resistance to photocorrosion, low cost, and low toxicity [1–4]. Nevertheless, its poor solar-light utilization, due to its band-gap value (3.0–3.2 eV) and high photo-charge-carrier recombination rate [5,6], limit the extensive application of anatase and rutile. These drawbacks were somewhat successfully overcome by TiO_2 dye-sensitization, doping, and coupling with other metals and their oxides [7–10]. The most promising method is the combination of TiO_2 with materials possessing narrow band-gaps. The resulting heterostructures (HSs) demonstrate an extended (to the visible-light spectrum) optical absorption and increased separation of charge carriers [11–14].

Bismuth (III)-containing oxides, such as Bi_2O_3, BiOI, BiOCl, $BiVO_4$, $Bi_4Ti_3O_{12}$, and Bi_2WO_6, have attracted much interest due to their superior photocatalytic and physico-chemical performances [15–18]. Importantly, Bi_2MoO_6 is a layered oxide with an Aurivillius

structure that possesses visible-light-driven photocatalytic activity for water and organic electrolysis and decomposition [19,20]. Interestingly, some studies reported that coupling Bi_2MoO_6 with TiO_2 yielded HSs with enhanced photocatalytic performance. For instance, the flake-like Bi_2MoO_6 grown on TiO_2 films demonstrated excellent significant visible-light self-cleaning properties [21], which were attributed to the synergy between the individual components of these HSs, including superhydrophilicity and effective charge-carrier separation [21]. Pan et al. [22] reported that Bi_2MoO_6/TiO_2 HS microspheres exhibited excellent photocatalytic activity towards phenol and nitrobenzene decomposition under visible light. Zhang et al. [23] prepared Bi_2MoO_6/TiO_2 HSs with two different morphologies using Bi_2MoO_6 nanoparticles and nanosheets. Both morphologies efficiently degraded organic pollutants because of the extended visible-light-absorption capability of Bi_2MoO_6 and excellent separation of charge carriers driven by the photo-induced potential differential of the Bi_2MoO_6/TiO_2 heterojunction [21–24]. A summary of Bi_2MoO_6-based photocatalysts and their photocatalytic performance is illustrated in Table S1 in the Supplementary Materials.

As is widely accepted, enhancement in the surface area could contribute to improving the photocatalytic performance because photodegradation is typically a surface-based process [25]. In this respect, one-dimensional (1D) nanomaterials, including nanowires, nanotubes, and nanorods, have attracted extensive attention because of their large aspect ratio, chemical stability, and unique geometrical morphologies, offering direct pathways for charge transport. On the one hand, nanomaterials with aligned 1D morphologies possess a short diffusion and transport path for holes, along with their radial directions. Simultaneously, their long axes are the preferred channels for electron transfer as well as optical scattering and adsorption [13,14]. Lindquist et al. [26] used Fe_2O_3 nanorod arrays as anodes in a photoelectrochemical (PEC) cell to address issues of the PEC system and improve its efficiency. Recent studies also demonstrated superior photocatalytic, photovoltaic, and PEC properties of the aligned 1D nanostructures in addition to their recyclable and reusable characteristics, unlike their bulk or randomly shaped (not aligned) counterparts [27–30]. On the other hand, nanomaterials with nanosheet morphologies could favor the adsorption of pollutants during photodegradation [31]. However, dispersed Bi_2MoO_6/TiO_2 nanoparticles have downsides owing to their tendency to agglomerate during the reaction and to the difficulty in separating and fully recovering them from the reaction mixture. Few studies have been published on HSs-containing Bi_2MoO_6 and 1D TiO_2 (Bi_2MoO_6/TiO_2 nanobelts, nanotubes, and nanorods) and their photocatalytic performance. Therefore, to further address and explore this topic, a strategy was developed to embed the photocatalytic species on a high surface area material [32,33]. In this context, we developed a simple hydrothermal/solvothermal method to synthesize HSs containing Bi_2MoO_6 nanosheets and TiO_2 nanorod arrays grown on an FTO surface in advance. The crystallinity, structure, morphology, band structure, and optical properties of these HSs were thoroughly analyzed. Our Bi_2MoO_6/TiO_2 HSs exhibited excellent photocatalytic activity in the visible-light region due to the combination of the Bi_2MoO_6 light-absorption and charge-separation efficiency of the Bi_2MoO_6/TiO_2 heterojunction.

2. Materials and Methods

2.1. Materials

All chemicals used in this study were of analytical grade, purchased from Sinopharm Chemical Reagent Co., Tianjing, China and used as received. FTO (SnO_2:F conducting glass), used as a substrate, was acquired from Kejing Materials Technology Co., Hefei, China. Deionized (DI) water, which was used throughout all experiments, was prepared in our laboratory using the water purifying system RC–K2 (Ruicheng Technology Co., Ltd., Beijing, China).

2.2. Preparation of TiO_2 Nanorod Arrays

TiO_2 nanorod arrays were grown on an FTO substrate hydrothermally [13,14]. First, a 1:1 (by volume) mixture of hydrochloric acid (HCl, AR, 36.0~38.0%) and DI water with

a specific $Ti(OC_4H_9)_4$ (AR, 98.0%) content was prepared. Then, the above solution was transferred to a Teflon pot, in which a rectangular piece of FTO, with the conducting layer facing down, was placed against the wall of the Teflon pot. Prior to the synthesis, the FTO was ultrasonicated in DI water, then in acetone, and finally in ethanol. The hydrothermal reaction was performed in a Teflon-lined, stainless-steel autoclave for 6 h at 453 K. The resulting product was TiO_2 nanorod arrays grown on the FTO pieces.

2.3. Synthesis of the Bi_2MoO_6/TiO_2 Composites

Bi_2MoO_6/TiO_2 composites were synthesized solvothermally [34–36]. The stepwise synthesis protocol is shown in Figure S1 in the Supplementary Materials. First, $Bi(NO_3)_3{\cdot}5H_2O$ (AR, 99.0%) and $Na_2MoO_4{\cdot}2H_2O$ (AR, 99.0%) (at 2:1 mole ratio) were dissolved in a mixture of ethylene glycol (EG, AR, 99.5%) and ethanol (C_2H_5OH, AR, 99.7%) (at 1:1 volume ratio) under constant stirring. Then, the resulting clear mixtures were placed into a 50 mL Teflon-lined, stainless-steel autoclave containing an FTO substrate coated with TiO_2 nanorod arrays. The reaction was conducted at 433 K for 14 h. Under these conditions, several Bi_2MoO_6/TiO_2 composites were prepared with different amounts of Bi_2MoO_6 by varying the mass of the raw materials, as shown in Table S2. The corresponding samples were marked as BMT-1, BMT-2, BMT-3, and BMT-4. In addition, pure Bi_2MoO_6 nanosheets (without TiO_2) were also synthesized under the same conditions.

2.4. Characterization

The phase structures of the as-prepared products were analyzed by X-ray diffraction (XRD) performed using a D8 Advance (Bruker Corp., Karlsruhe, Germany) instrument equipped with Cu Kα radiation as an X-ray source. The sample morphologies were inspected using scanning electron microscopy (SEM) performed with a JSM-7100F (Hitachi Corp., Tokyo, Japan) instrument. The elemental composition and valence-band potential (E_{VB}) were obtained using X-ray photoelectron spectroscopy (XPS) performed with an ESCALAB 250 (Thermo Scientific (Shanghai) Corp., China) instrument equipped with Al Kα radiation as an X-ray source. The ultraviolet-visible (UV–Vis) absorption spectra were recorded by a UV2600 (Shimadzu (China) Corp., Shanghai, China) spectrophotometer. The Brunauer–Emmett–Teller (BET) specific surface areas (S_{BET}) and pore volume of the as-prepared samples were estimated from the nitrogen adsorption−desorption isotherms that were recorded by a nitrogen adsorption apparatus (ASAP 2020, Micromeritics Instruments Corp., Atlanta, GA, USA) at 77 K. Electron spin resonance (ESR) signals of the radicals' spin were recorded by a E500 spectrometer (Bruker Corp., Karlsruhe, Germany). The 5,5-dimethyl-1-pyrroline N-oxide (DMPO) was selected as a free radical scavenger to capture ·OH and $\cdot O_2^-$ species. Photoluminescence (PL) emission spectra were measured at room temperature using a FluoTime-300 spectrophotometer (PicoQuant Co., Berlin, Germany) under a 325 nm laser as an excitation source.

2.5. Photocatalytic Activity

Methylene blue (MB) was used as a compound representing organic pollutants and other organic dyes. MB is chemically stable and difficult to decompose. The photocatalytic degradation was tested in a MB aqueous solution (1.0×10^{-5} mol·L^{-1}, 50 mL) using a 1×1 cm^2 FTO substrate containing the Bi_2MoO_6/TiO_2 HSs. A blank sample (without any catalysts) and TiO_2/FTO nanorod arrays were also used for comparison for the photocatalytic MB degradation experiments. AM 1.5 G simulated solar light (with 100 mW/cm^2 fluence) was provided by a 300 W Xe PLS-SXE300D (Perfectlight Technology Co., Beijing, China) lamp. Prior to the photocatalytic experiments, the aqueous solutions containing MB and photocatalysts were kept in the dark for 30 min to establish an adsorption/desorption equilibrium. Absorption spectra of MB aqueous solutions, at a wavelength of 664 nm, were collected using a UV–Vis spectrophotometer at specific intervals, which revealed the

changes in MB content after irradiation. The dye degradation efficiency was calculated by the formula below [37]:

$$X = \frac{C}{C_0} \times 100\%$$

where C_0 and C are MB contents at times 0 and t, respectively.

2.6. Assessment of PEC Performance

The PEC performance of our samples was tested using a CHI660E (Chenhua Instruments Inc., Shanghai, China) electrochemical workstation equipped with a three-electrode (Pt foil as a counter, calomel as a reference, and working electrodes) configuration. In addition, 0.5 M Na_2SO_4 served as an electrolyte. The effective area of the working electrodes was 1.5 cm^2. Electrochemical-impedance-spectroscopy (EIS) was performed with a 5 mV amplitude AC voltage in the 10 Hz–1 MHz range. Mott–Schottky plots of pure TiO_2 and Bi_2MoO_6 were recorded at 1000 Hz. The light source was the same as in the photocatalytic experiment.

3. Results and Discussion

3.1. X-ray Diffraction (XRD)

As shown in Figure 1, synthesized TiO_2, Bi_2MoO_6, and Bi_2MoO_6/TiO_2 composite films possessed good crystallinity according to the XRD results. The XRD pattern revealed diffraction peaks at 36.2°, 54.3°, and 62.8°, attributed to (101), (211), and (002) crystal planes of rutile TiO_2, respectively (PDF card number 21-1276). The XRD patterns of Bi_2MoO_6/TiO_2 revealed TiO_2 and FTO peaks, as well as peaks at 28.2°, 32.5°, 46.7°, and 55.5°, that were attributed to (131), (200)/(002), (202), and (133) planes of the orthorhombic koechlinite phase of Bi_2MoO_6, according to PDF card number 76-2388. These results confirmed the formation of Bi_2MoO_6/TiO_2 composites. XRD peaks of Bi_2MoO_6 observed in the Bi_2MoO_6/TiO_2 spectra became sharper and narrower as the initial Bi_2MoO_6 amount was increased, while the XRD peaks of TiO_2 became less intense. No other changes in the crystalloid structure were observed as the initial materials used were changed.

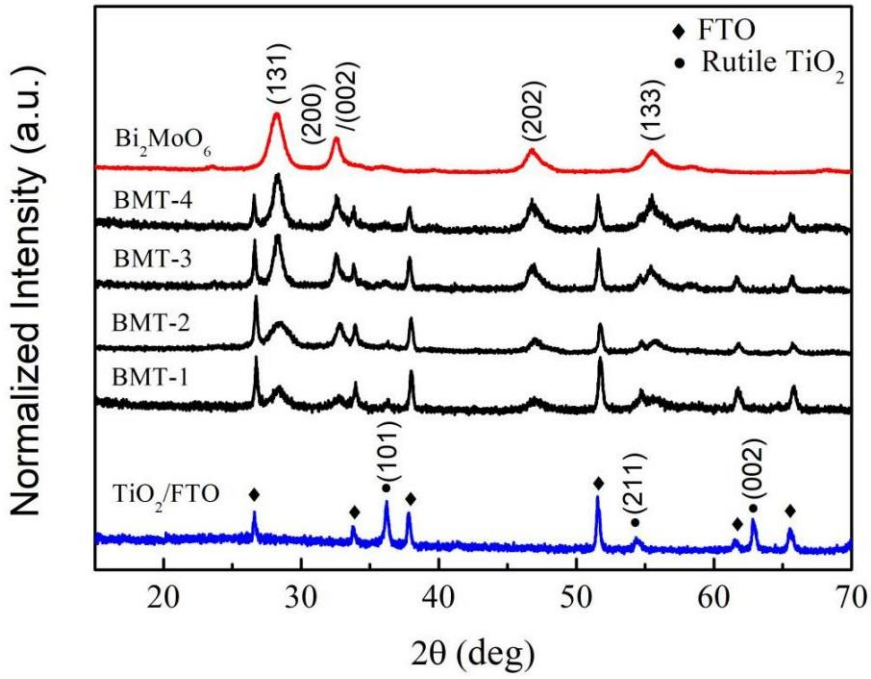

Figure 1. XRD patterns of pristine TiO_2/FTO, Bi_2MoO_6, and BMT-1, BMT-2, BMT-3, and BMT-4 samples.

3.2. X-ray Photoelectron Spectroscopy (XPS)

XPS of the BMT-3 composites revealed the presence of Bi, Mo, Ti, and O elements (see Figure 2a). Some carbon was also observed due to environmental and instrument contamination. The high-resolution Bi 4*f* XPS spectrum showed two peaks at 158.0 and 163.3 eV (see Figure 2b), which were assigned to the spin-orbit splitting peaks of Bi $4f_{7/2}$ and Bi $4f_{5/2}$, respectively [38]. Thus, Bi in Bi_2MoO_6/TiO_2 existed as Bi^{3+}. Two strong peaks at 232.3 and 235.5 eV, corresponding to Mo $3d_{5/2}$ and Mo $3d_{3/2}$ spin-orbit components of Mo^{6+}, respectively [39] (see Figure 2c), were observed in the high-resolution Mo 3*d* XPS spectrum. The peaks at 457.5 and 463.2 eV matched the binding energies of Ti $2p_{3/2}$ and Ti $2p_{1/2}$ states, respectively (see Figure 2d). Thus, Ti was present as Ti^{4+} in the Bi_2MoO_6/TiO_2 composites. The fitting of the high-resolution O 1*s* XPS spectrum revealed three peaks at 528.9, 529.4, and 531.1 eV (see Figure 2e), which corresponded to Bi-O, Mo-O, and Ti-O bonds, respectively [22,38]. Thus, these results confirmed the coexistence of Bi_2MoO_6 and TiO_2 in the synthesized HSs.

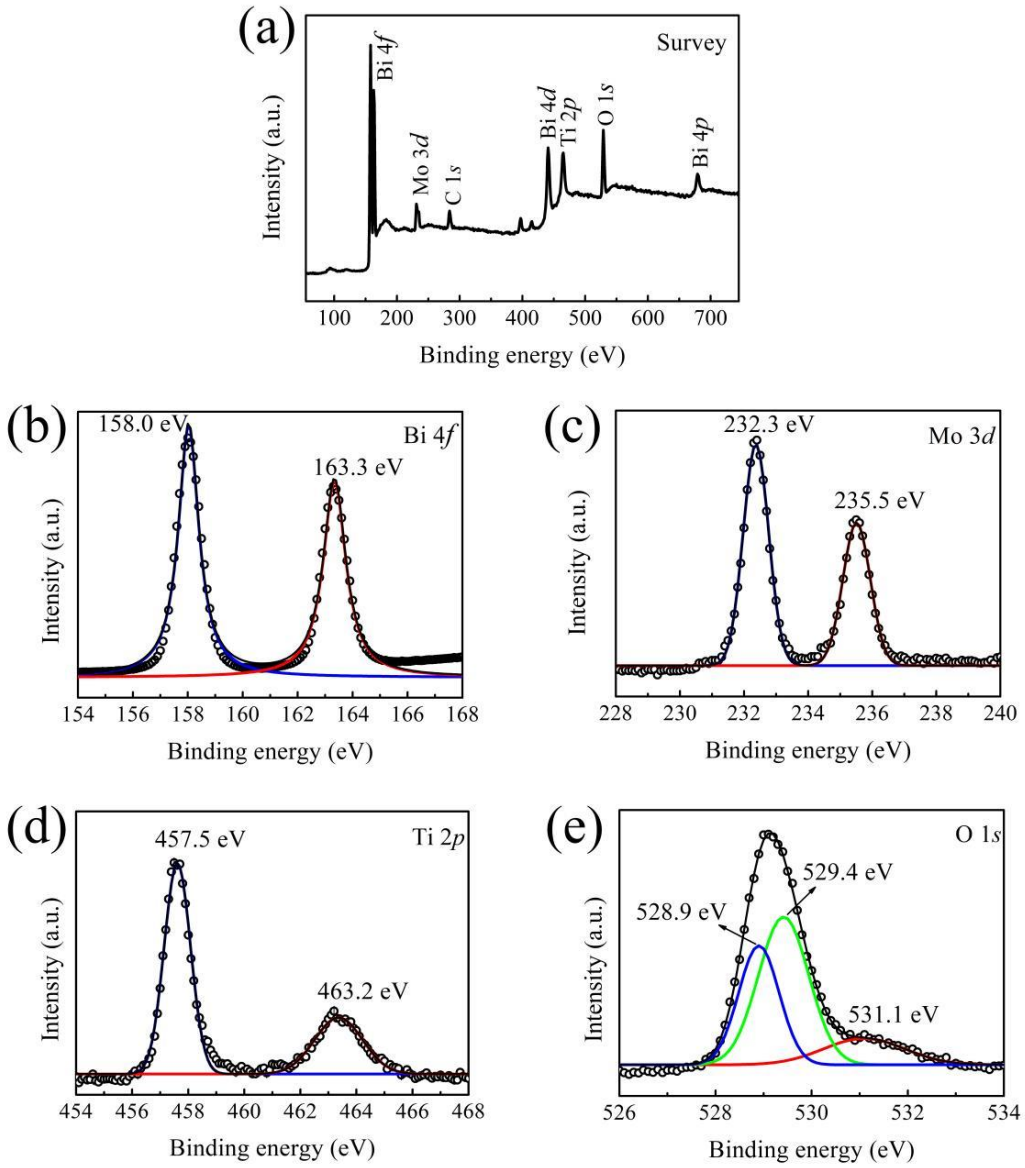

Figure 2. (**a**) XPS fully scanned spectrum of the BMT-3 composite, and high-resolution XPS of (**b**) Bi 4*f*, (**c**) Mo 3*d*, (**d**) Ti 2*p*, and (**e**) O 1*s*. The circle symbol represent the experimental data, the black lines represent the fitting curves, and the colored lines represent the multimodal fitting curves.

3.3. Morphologies

SEM showed that the diameters of the bare TiO_2 nanorods were 200 nm (see Figure 3a). Moreover, the nanorods were vertically aligned and uniformly distributed on the FTO substrate. Pure Bi_2MoO_6 nanosheets exhibited laminar and irregular, sheet-like morphology (see Figure 3b). SEM of the Bi_2MoO_6/TiO_2 composites showed that some Bi_2MoO_6 nanosheets adhered to the TiO_2 nanorods (see Figure 3c–f). Additionally, as the initial Bi/Mo content was increased, the Bi_2MoO_6 nanosheets increased in number and began to aggregate. The sample (BMT-3, shown in Figure 3e) with appropriate initial Bi/Mo content showed the growth of dispersed Bi_2MoO_6 nanosheets around TiO_2 nanorods. Instead, a serious agglomeration of Bi_2MoO_6 was observed, as shown in Figure 3f. These findings suggest that the initial concentration of the materials used significantly affected the Bi_2MoO_6/TiO_2 composite morphology.

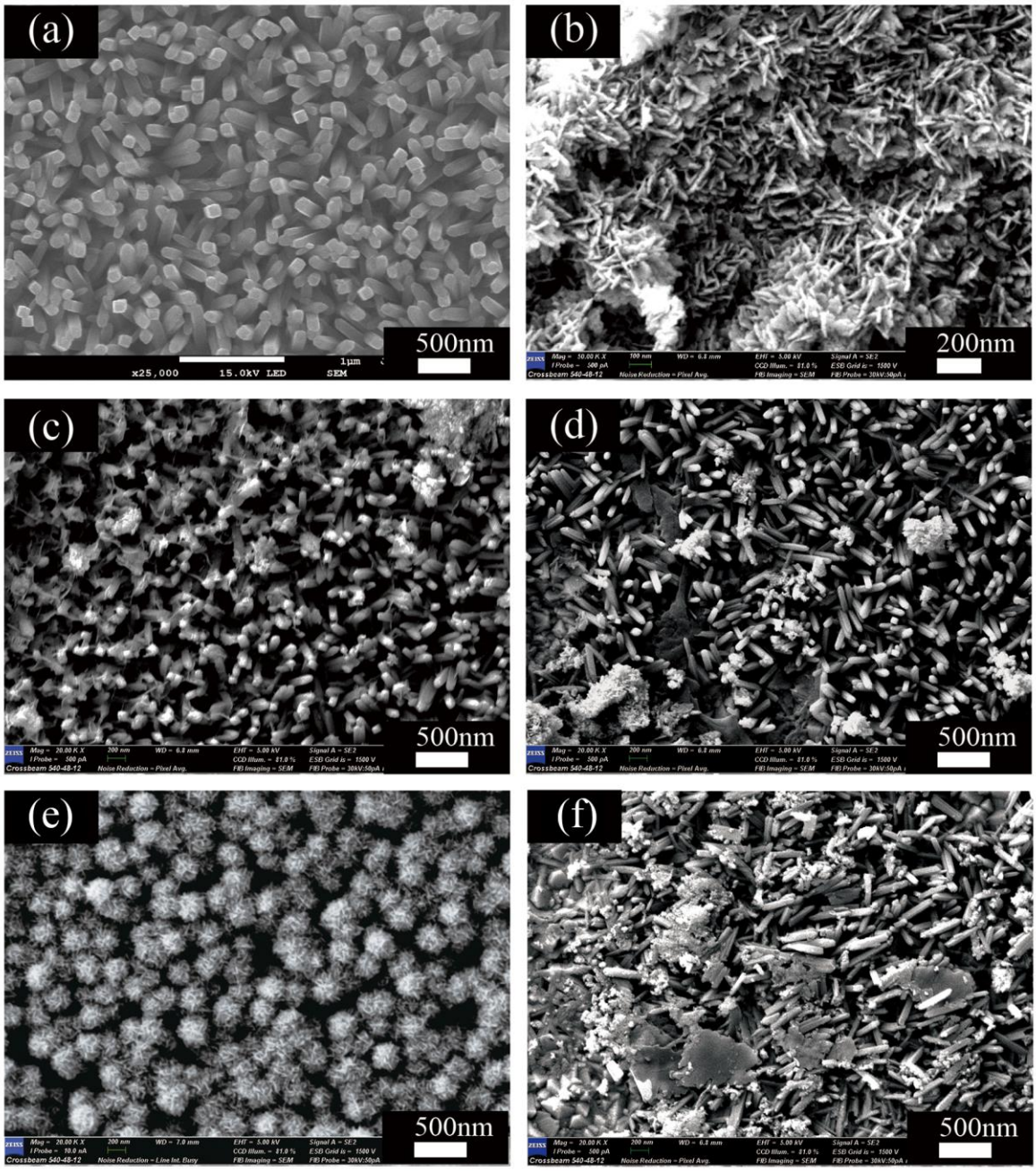

Figure 3. SEM images of (**a**) pristine TiO_2 nanorod arrays, (**b**) pure Bi_2MoO_6 nanosheets, and Bi_2MoO_6/TiO_2 composites denoted as (**c**) BMT-1, (**d**) BMT-2, (**e**) BMT-3, and (**f**) BMT-4.

It is widely known that the photocatalytic activity of catalysts is significantly influenced by the specific surface area and pore volume of photocatalysts due to the presence of surface-reactive sites [40]. The nitrogen adsorption−desorption isotherms of the TiO_2, Bi_2MoO_6, BMT-3, and BMT-4 samples are shown in Figure S2 in the Supplementary Materials. The similar adsorption−desorption curves revealed strong N_2 adsorption−desorption performance, which indicated the existence of capillary condensation in the large mesopores in the samples. The S_{BET} and pore volume of TiO_2, Bi_2MoO_6, BMT-3, and BMT-4 HSs are listed in Table S3. Interestingly, the coupling of TiO_2 and Bi_2MoO_6 significantly increased the S_{BET} and pore volume (the maximum value for BMT-3 are 88.2 m^2/g and 0.18 cm^3/g, respectively) compared to the pure Bi_2MoO_6 (26.0 m^2/g and 0.05 cm^3/g, respectively). Combined with the photocatalytic experiment results we can deduce that the high S_{BET} and pore volume of BMT-3 played significant roles in enhancing photocatalytic performance.

3.4. Optical Properties

The UV–Vis spectra of TiO_2 nanorod arrays showed that they were adsorbed, as expected, in the ultraviolet region at 400 nm (see Figure 4a), which is mainly accounted for by absorption within the rutile band-gap [41]. The absorption intensity of Bi_2MoO_6 was relatively mild and peaked at ~450 nm. Thus, a slight extension to the visible-light region was observed in comparison to TiO_2. The absorption edges of the Bi_2MoO_6/TiO_2 composites exhibited a certain degree of red-shift, which indicates the extension of the material's absorption towards visible light. The band-gap energies of the TiO_2, Bi_2MoO_6, and Bi_2MoO_6/TiO_2 HSs were calculated from the Kubelka–Munk function, plotted against the photon energy (see Figure 4b). The band-gap values of TiO_2 and Bi_2MoO_6 were equal to 3.1 and 2.77 eV, respectively. Moreover, the band-gap values of the BMT-1, BMT-2, BMT-3, and BMT-4 composites were 2.88, 2.85, 2.81, and 2.79 eV, respectively. Furthermore, the photogenerated electron-hole pairs were excited due to the extension of absorption into the visible-light region, favoring enhanced PEC and photocatalytic performance.

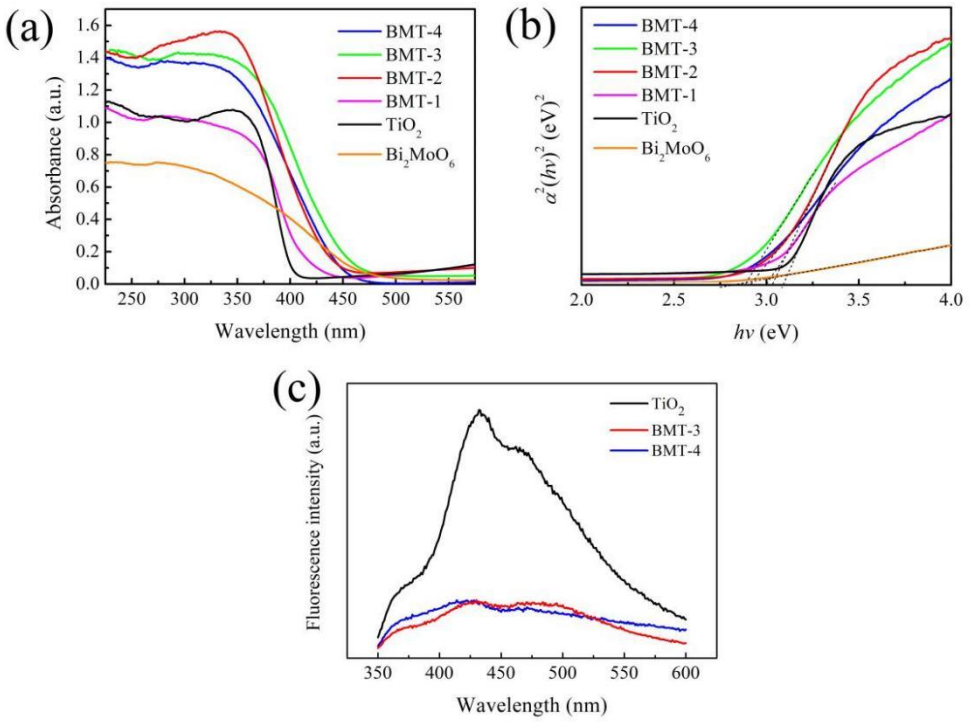

Figure 4. (**a**) UV–Vis absorption spectra: (**b**) Kubelka–Munk plots of pristine TiO_2 nanorod arrays, pure Bi_2MoO_6, and Bi_2MoO_6/TiO_2 composites; and (**c**) PL spectra of TiO_2 and Bi_2MoO_6/TiO_2 HSs photocatalysts.

Photoluminescence (PL) emission spectra have been widely employed to reveal the separation efficiency of the photo-induced electrons and holes in the composite semiconductors [42]. The PL spectra of the as-prepared TiO_2, BMT-3, and BMT-4 samples in the present study are shown in Figure 4c. The strongest emission intensity peak observed in pure TiO_2 nanorods corresponded to the band-gap transition. A significant decrease in fluorescence of Bi_2MoO_6/TiO_2 (BMT-3 and BMT-4) was observed, indicating a lower photoelectron-hole recombination in Bi_2MoO_6/TiO_2 than in TiO_2. Moreover, the similar fluorescence intensity of BMT-3 and BMT-4 indicated similar separation performance of the photo-induced electrons and holes in the BMT-3 and BMT-4 samples. The migration and recombination efficiencies of the photo-induced carriers in all samples were further revealed by EIS characterization.

3.5. Photocatalytic Properties

The relationship between residual MB contents and irradiation time, with and without photocatalyst, is shown in Figure 5a. Figure 5b shows the fitting curves of the kinetics of MB photodegradation. The degradation of MB in the presence of TiO_2 and Bi_2MoO_6/TiO_2 obeyed the pseudo-first-order kinetics and could be expressed as $\ln(C/C_0) = k(t-t_0)$, where k is the reaction rate constant [43,44]. The rate constants and the corresponding correlation coefficients (R-Square) of different photocatalysts and the blank sample are given in Table S4, which were calculated by linear fitting $-\ln(C/C_0)$ to irradiation time (t). The values of R-Square are close to 1, which reveal a good correlation to the pseudo-first-order reaction kinetics. MB degradation without catalysts was negligible under visible light, with a k value of 0.000538 min^{-1} (see Figure 5b). In contrast, the reaction rate constant of MB decomposition in the presence of TiO_2 nanorods was 0.00113 min^{-1}, which was attributed to the photon-trapping effect caused by the morphology of the TiO_2 nanostructure [13,14]. However, the photocatalytic performances of the Bi_2MoO_6/TiO_2 HSs were significantly better. Thus, the presence of Bi_2MoO_6 in the composite played a significant role. The photocatalytic ability of Bi_2MoO_6/TiO_2 (BMT-4) was lower for samples with higher Bi_2MoO_6 content because of the recombination of the photogenerated electron-hole pairs inside the numerous Bi_2MoO_6 nanosheets [44]. From the viewpoint of practical application, it is important to evaluate the stability of the as-prepared catalyst. Comparison of the XRD pattern of the Bi_2MoO_6/TiO_2 (BMT-3) before and after the photocatalytic reaction (performed three times with the same catalyst) showed that, even after three cycles, the positions and intensities of the XRD peaks remained almost the same (Figure 5c), which confirmed the excellent stability of the Bi_2MoO_6/TiO_2 composite catalysts. The stable activity was further validated by repeating the photocatalytic degradation processes thrice, as shown in Figure 5d. The three degradation curves showed a similar trend in each running cycle, which indicated that the Bi_2MoO_6/TiO_2 photocatalyst exhibited high and stable activity for degradation.

To investigate the mechanisms underlying the photo-oxidation ability, ESR technology was used to detect active free radicals. The ESR signals of BMT-3 dispersed in the DMPO solution are shown in Figure S3. No ·OH ESR signals were generated in darkness; however, a set of four feature peaks with an intensity ratio of 1:2:2:1 were observed after light illumination (see Figure S3a), attributed to DMPO-·OH adducts. Similarly, no $\cdot O_2^-$ signals were generated in the dark, and six peaks of DMPO-$\cdot O_2^-$ were observed in the ESR spectra (see Figure S3b) with illumination. These results demonstrated that $\cdot O_2^-$ and ·OH are both active species, and their synergistic effect significantly promoted the photocatalytic degradation of MB.

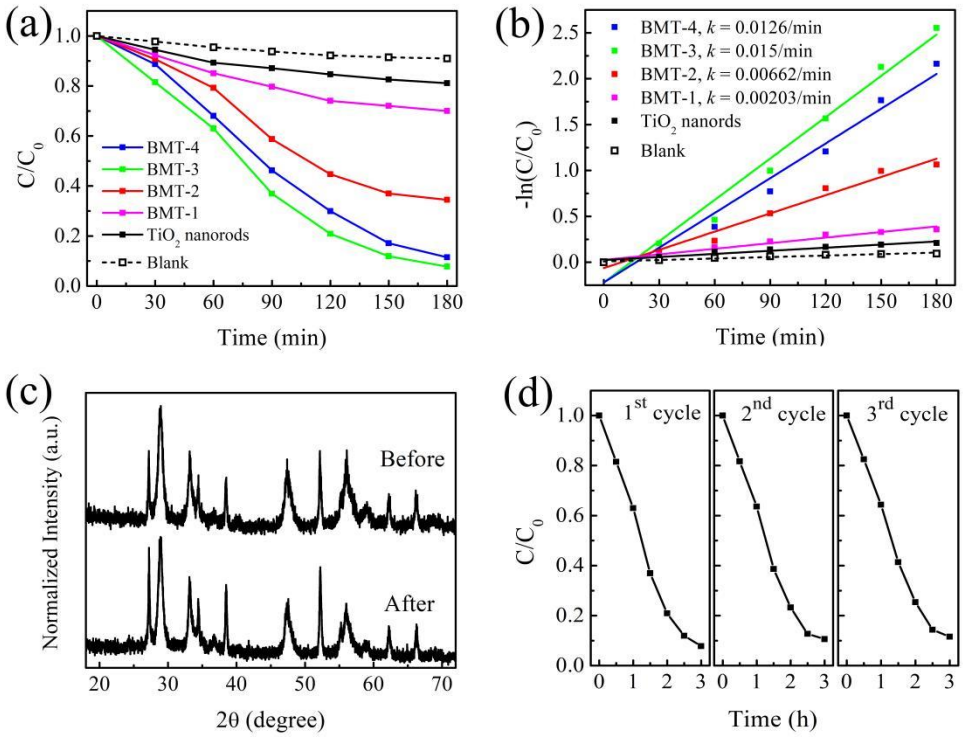

Figure 5. (**a**) Normalized MB concentration versus the irradiation time; (**b**) Kinetic curves of MB photodegradation; (**c**) XRD patterns of original BMT-3 sample and after three recycles photodegradation; (**d**) Repeated photocatalytic activity of BMT-3 under visible-light irradiation for MB degradation.

3.6. PEC Analysis

The PEC performance of the Bi_2MoO_6/TiO_2 HSs was compared to that of pure TiO_2 nanorod arrays and Bi_2MoO_6. For this purpose, we recorded the photocurrent as a function of time (*I*–*t* curves) by alternating exposure to darkness and visible light (see Figure 6a). All samples exhibited similar photocurrent responses. No photocurrent was observed in the dark, which confirmed the absence of any electrochemical processes. A minimal photocurrent response was observed for the TiO_2 nanorod array, and a significant one for the Bi_2MoO_6/TiO_2 HSs. The BMT-3 sample exhibited optimal stability and reproducibility of the photocurrent response since the Bi_2MoO_6/TiO_2 HSs, and the amount of Bi_2MoO_6 was the most favorable out of all the BMT samples. The separation and collection efficiency of interface charges were further studied by EIS (see Figure 6b). Typically, the semicircles in the corresponding Nyquist plots corresponded to Faradic reactions. It has been established that the semicircle radius is negatively correlated with the charge transfer efficiency [45,46]. In our study, the semicircle diameters for the Bi_2MoO_6/TiO_2 HSs were significantly smaller than those obtained for Bi_2MoO_6 and TiO_2. This data confirms the lower interfacial charge-transfer resistance and fast charge-transfer process of our composite Bi_2MoO_6/TiO_2 HSs due to the presence of Bi_2MoO_6 and its interfacial interaction with TiO_2, which enhanced the separation and transfer efficiency of the electron-hole pairs photogenerated in the Bi_2MoO_6/TiO_2 HSs. The heterojunction of the Bi_2MoO_6/TiO_2 interface suppressed the charge recombination, thereby producing more (re)active species, which resulted in a high photocurrent response and photocatalytic activity.

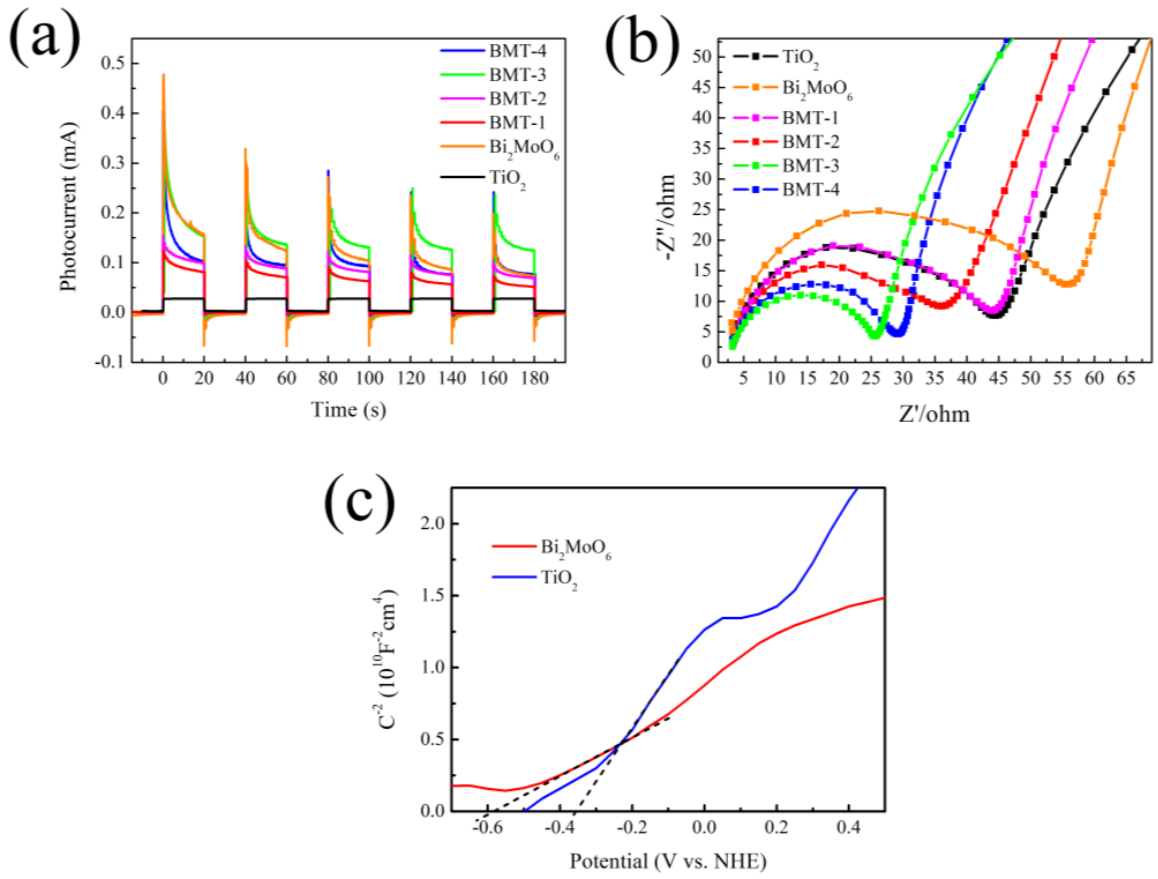

Figure 6. (**a**) The transient photocurrent response; (**b**) Nyquist plots of pristine TiO_2, Bi_2MoO_6, and Bi_2MoO_6/TiO_2; (**c**). Mott–Schottky plots of pristine TiO_2 and Bi2MoO6.

The Mott–Schottky plots of TiO_2 and Bi_2MoO_6 are shown in Figure 6c. The positive slopes of both compounds imply that they are n-type semiconductors. The flat-band potential (V_{fb}) can be calculated by the Mott–Schottky equation [42]:

$$\frac{1}{C^2} = \frac{2}{e\varepsilon\varepsilon_0 N_d}[(V - V_{fb}) - \frac{kT}{e}]$$

where C is the capacitance at the interface with the electrolyte, e is the electronic charge, ε_0 is the vacuum permittivity, ε is the sample dielectric constant, N_d is the charge-carrier concentration, V and V_{fb} are the applied and flat-band potentials, k is the Boltzmann's constant, and T is the temperature [47]. The V_{fb} could be calculated from the intercept of the $1/C^2$ curve (plotted as a V function) with the x-axis [48]. The V_{fb} values for the pure TiO_2 and Bi_2MoO_6 were equal to -0.35 and -0.58 V (vs. a normal hydrogen electrode, NHE), respectively.

3.7. Energy Band Alignment and Photocatalytic Mechanism

In order to explain the photocatalytic process, the energy band alignment of the Bi_2MoO_6/TiO_2 HSs was investigated. Mott–Schottky plots revealed the flat-band potential of TiO_2 and Bi_2MoO_6 (Figure 6c). A gap between E_{VB} and flat-band potential can be inferred from the XPS–valance band (XPS–VB) plots, as shown in Figure S4. Thus, the calculated E_{VB} values of TiO_2 and Bi_2MoO_6 were 2.4 and 1.68 V, respectively. Moreover, the conduction band potential (E_{CB}) of TiO_2 and Bi_2MoO_6 were calculated to be -0.7 and -1.09 V, respectively. Based on these results, the band alignment of the Bi_2MoO_6/TiO_2 was established, as shown in Figure 7. The E_{CB} and E_{VB} of TiO_2 were more positive than those of Bi_2MoO_6. Accordingly, it is highly likely that Bi_2MoO_6/TiO_2 HSs possess staggered band

alignment. Visible-light irradiation excites Bi_2MoO_6 molecules, generating electron-hole pairs. At the same time, a large band-gap prevents TiO_2 molecules from being excited by visible-light irradiation. In this case, the electrons travel from the conduction band of the Bi_2MoO_6 to TiO_2, which suppresses electron-hole pair recombination by the internal field of the Bi_2MoO_6/TiO_2 heterojunction since the E_{CB} of Bi_2MoO_6 is relatively more negative. The separated electrons can react with O_2 molecules, forming $\cdot O_2^-$ radicals since the corresponding redox potential is equal to -0.046 V and more positive than the E_{CB} of TiO_2. Subsequently, the H_2O molecules are transformed into ·OH radicals after trapping an electron. Both photogenerated holes, together with $\cdot O_2^-$ and ·OH radicals, can react with MB molecules, damaging their structures. We believe that this process, based on the interfacial charge transfer, is indeed feasible. The reaction mechanism and chemical equations of the above processes are proposed as follows and can be found in the previous literature [23,38,49,50].

$$Bi_2MoO_6 + h\nu \rightarrow Bi_2MoO_6\ (e^- + h^+)$$

$$Bi_2MoO_6\ (e^- + h^+) + TiO_2 \rightarrow Bi_2MoO_6\ (h^+) + TiO_2\ (e^-)$$

$$TiO_2\ (e^-) + O_2 \rightarrow TiO_2 + \cdot O_2^-$$

$$\cdot O_2^- + H_2O \rightarrow \cdot HO_2 + OH^-$$

$$\cdot HO_2 + H_2O \rightarrow H_2O_2 + \cdot OH$$

$$H_2O_2 \rightarrow 2\cdot OH$$

$$Bi_2MoO_6\ (h^+) + MB \rightarrow \text{degraded products}$$

$$\cdot O_2^- + MB \rightarrow \text{degraded products}$$

$$\cdot OH + MB \rightarrow \text{degraded products}$$

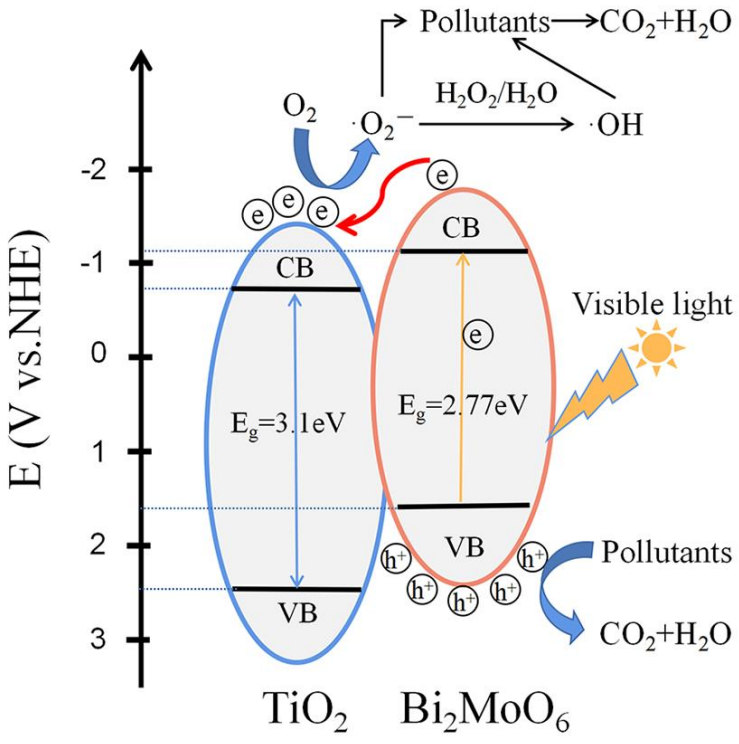

Figure 7. The band structures of the Bi_2MoO_6/TiO_2 HSs and postulated photocatalytic mechanism of dye degradation.

4. Conclusions

In summary, the Bi_2MoO_6/TiO_2 HSs were synthesized through a simple two-step solvothermal process by growing Bi_2MoO_6 nanosheets on TiO_2 nanorod arrays. The Bi_2MoO_6/TiO_2 HSs exhibited enhanced photocatalytic activity for MB degradation under visible-light irradiation, and BMT-3 achieved the highest degradation rate of k = 0.015 min^{-1} among all samples. The enhancement was attributed to the heterojunction structures established by the close contact between the Bi_2MoO_6 nanosheets and the TiO_2 nanorods. The results of the UV–Vis absorption spectra show an extended absorption to visible light after coupling Bi_2MoO_6 with TiO_2. The results of N_2 adsorption−desorption isotherms show a significantly increased S_{BET} and pore volume compared to the pure Bi_2MoO_6 due to the hierarchical structure of the Bi_2MoO_6/TiO_2 HSs. The results of PL and PEC characterization of the Bi_2MoO_6/TiO_2 HSs reveal improved separation efficiency and enhanced migration rate of photogenerated electron-hole pairs. Thus, the synergy between Bi_2MoO_6 and TiO_2 was identified as the crucial factor leading to the improved photocatalytic performance. Furthermore, the reusability and chemical stability of Bi_2MoO_6/TiO_2 HSs is demonstrated by photocatalytic cycle test. Finally, the mechanism and process of the dye photodegradation were discussed. The h^+, $\cdot O_2^-$, and ·OH radicals were validated as being active species that react with MB dye molecules. The results of this work suggest that Bi_2MoO_6/TiO_2 HSs are promising candidate materials for wastewater treatment. Collectively, our current strategy can help in the synthesis and photocatalytic application of other heterostructures in the future.

Supplementary Materials: The following supporting information can be downloaded at: https://www.mdpi.com/article/10.3390/nano12030574/s1. Table S1: Bi_2MoO_6-based photocatalysts and their photocatalytic performance; Table S2: The abbreviations of products with different amounts of Bi_2MoO_6 by varying the mass of raw materials in precursor solution; Table S3: S_{BET}, Pore Volume, and Mean Pore Diameter of TiO_2, Bi_2MoO_6, BMT-3, and BMT-4 samples; Table S4: Pseudo-first-order rate constants and corresponding R-Square values of different samples; Figure S1: Stepwise synthesis protocol of TiO_2 nanorod arrays and Bi_2MoO_6/TiO_2 HSs; Figure S2: N2 adsorption−desorption isotherms (a) and the corresponding pore-size distribution curves (b) of TiO_2, Bi_2MoO_6, BMT-3, and BMT-4 samples; Figure S3: The ESR signals of ·OH (a) and $\cdot O_2^-$ radicals (b) of BMT-3 photocatalysts; Figure S4: XPS valence-band spectra of TiO_2 and Bi_2MoO_6.

Author Contributions: Conceptualization, D.Z. and Z.H.; Data curation, Y.T., Y.F., and Y.Z.; Formal analysis, Y.T., Y.F., and Y.Z.; Funding acquisition, G.Z.; Investigation, R.D. and S.G.; Methodology, R.D.; Resources, G.Z.; Supervision, D.Z.; Visualization, S.G.; Writing–original draft, D.Z.; Writing–review and editing, D.Z. and Z.H. All authors have read and agreed to the published version of the manuscript.

Funding: This work is supported by the National Natural Science Foundation of China (Grant Numbers: 61575085 and 61240056) and guidance project of the science and technology research of the Education Department of Hubei Province (Grant Number: B2019235).

Data Availability Statement: All data generated or analyzed during this study are contained within the article and supplementary materials.

Conflicts of Interest: The authors declare no conflict of interest.

References

1. Fujishima, A.; Honda, K. Electrochemical photolysis of water at a semiconductor electrode. *Nature* **1972**, *238*, 37–38. [CrossRef] [PubMed]
2. Schrauzer, G.N.; Guth, T.D. Photolysis of water and photoreduction of nitrogen on titanium dioxide. *J. Am. Chem. Soc.* **1977**, *99*, 7189–7193. [CrossRef]
3. Kraeutler, B.; Bard, A.J. Heterogeneous photocatalytic preparation of supported catalysts. Photodeposition of platinum on titanium dioxide powder and other substrates. *J. Am. Chem. Soc.* **1978**, *100*, 4317–4318. [CrossRef]
4. Fujishima, A.; Hashimoto, K.; Watanabe, T. *TiO_2 Photocatalysis: Fundamentals and Applications*; BKC, Inc.: Tokyo, Japan, 1999.
5. Tang, H.; Prasad, K.; Sanjinbs, R.; Schmid, P.E.; Levy, F. Electrical and optical properties of TiO_2 anatase thin films. *J. Appl. Phys.* **1994**, *75*, 2042–2047. [CrossRef]

6. Yadav, H.M.; Kim, J.S.; Pawar, S.H. Developments in photocatalytic antibacterial activity of nano TiO_2: A review. *Korean J. Chem. Eng.* **2016**, *33*, 1989–1998. [CrossRef]
7. Sahare, S.; Veldurthi, N.; Singh, R.; Swarnkar, A.K.; Bhave, T. Enhancing the efficiency of flexible dye-sensitized solar cells utilizing natural dye extracted from Azadirachta indica. *Mater. Res. Express* **2015**, *2*, 105903. [CrossRef]
8. Grabowska, E.; Reszczyńska, J.; Zaleska, A. Mechanism of phenol photodegradation in the presence of pure and modified-TiO_2: A review. *Water Res.* **2012**, *46*, 5453–5471. [CrossRef]
9. Mohamed, M.A.; Jaafar, J.; Zain, M.F.M.; Minggu, L.J.; Kassim, M.B.; Salehmin, M.N.I.; Rosmie, M.S.; Salleh, W.N.W.; Othman, M.H.D. Concurrent growth, structural and photocatalytic properties of hybridized C, N co-doped TiO_2 mixed phase over g-C3N4 nanostructured. *Scr. Mater.* **2018**, *142*, 143–147. [CrossRef]
10. Saber, N.B.; Mezni, A.; Alrooqi, A.; Altalhi, T. Fabrication of efficient Au@TiO_2/rGO heterojunction nanocomposite: Boosted photocatalytic activity under ultraviolet and visible light irradiation. *J. Mater. Res. Technol.* **2021**, *12*, 2238–2246. [CrossRef]
11. Ismael, M. A review and recent advances in solar-hydrogen energy conversion based on photocatalytic water splitting over doped-TiO_2 nanoparticles. *Sol. Energy* **2020**, *211*, 522–546. [CrossRef]
12. Pham, V.V.; Phat, B.D.; Huy, T.H.; Cao, M.T.; Le, V.H. Photoreduction route for Cu_2O/TiO_2 nanotubes junction for enhanced photocatalytic activity. *RSC Adv.* **2018**, *8*, 12420–12427. [CrossRef]
13. Fu, Y.; Mao, Z.P.; Zhou, D.; Hu, Z.L.; Tu, Y.F.; Tian, Y.; Zheng, G. Fabrication of Ni-doped PbTiO3-coated TiO_2 nanorod arrays for improved photoelectrochemical performance. *J. Nanomater.* **2019**, *11*, 2019. [CrossRef]
14. Fu, Y.; Mao, Z.P.; Zhou, D.; Hu, Z.L.; Zheng, G. Preparation of $BiFeO_3$-overcoated TiO_2 nanorod arrays for the enhanced visible-light activity. *Mater. Res. Express* **2019**, *6*, 1050c6. [CrossRef]
15. Liu, X.; Gu, S.; Zhao, Y.; Zhou, G.; Li, W. $BiVO_4$, Bi_2WO_6 and Bi_2MoO_6 photocatalysis: A brief review. *J. Mater. Sci. Technol.* **2020**, *56*, 45–68. [CrossRef]
16. Chai, S.Y.; Kim, Y.J.; Jung, M.H.; Chakraborty, A.K.; Jung, D.; Lee, W.I. Heterojunctioned $BiOCl/Bi_2O_3$, a new visible light photocatalyst. *J. Catal.* **2009**, *262*, 144–149. [CrossRef]
17. Xiang, Z.; Wang, Y.; Zhang, D.; Ju, P. $BiOI/BiVO_4$ p-n heterojunction with enhanced photocatalytic activity under visible-light irradiation. *J. Ind. Eng. Chem.* **2016**, *40*, 83–92. [CrossRef]
18. Wei, W.; Dai, Y.; Huang, B. First-principles characterization of Bi-based photocatalysts: $Bi_{12}TiO_{20}$, Bi_2Ti2O_7, and $Bi_4Ti_3O_{12}$. *J. Phys. Chem. C* **2009**, *113*, 5658–5663. [CrossRef]
19. Yu, H.; Jiang, L.; Wang, H.; Huang, B.; Zeng, G. Photocatalysis: Modulation of Bi_2MoO_6-based materials for photocatalytic water splitting and environmental application: A critical review. *Small* **2019**, *15*, 1901008. [CrossRef] [PubMed]
20. Peng, Y.; Liu, Q.; Zhang, J.; Zhang, Y.; Geng, M.; Yu, J. Enhanced visible-light-driven photocatalytic activity by 0D/2D phase heterojunction of quantum dots/nanosheets on bismuth molybdates. *J. Phys. Chem. C.* **2018**, *122*, 3738–3747. [CrossRef]
21. Tian, G.; Chen, Y.; Zhai, R.; Zhou, J.; Zhou, W.; Wang, R.; Pan, K.; Tiana, C.; Fu, H. Hierarchical flake-like Bi_2MoO_6/TiO_2 bilayer films for visible-light-induced self-cleaning applications. *J. Mater. Chem. A* **2013**, *1*, 6961–6968. [CrossRef]
22. Li, J.; Liu, X.; Sun, Z.; Pan, L. Novel Bi_2MoO_6/TiO_2 heterostructure microspheres for degradation of benzene series compound under visible light irradiation. *J. Colloid Interface Sci.* **2016**, *463*, 145–153. [CrossRef] [PubMed]
23. Zhang, M.; Shao, C.; Mu, J.; Zhang, Z.; Guo, Z.; Zhang, P.; Liu, Y. One-dimensional Bi_2MoO_6/TiO_2 hierarchical heterostructures with enhanced photocatalytic activity. *CrystEngComm* **2012**, *14*, 605–612. [CrossRef]
24. Li, L.; Salvador, P.A.; Rohrer, G.S. Photocatalysts with internal electric fields. *Nanoscale* **2014**, *6*, 24–42. [CrossRef] [PubMed]
25. Sharma, S.; Basu, S. Highly reusable visible light active hierarchical porous WO_3/SiO_2 monolith in centimeter length scale for enhanced photocatalytic degradation of toxic pollutants. *Sep. Purif. Technol.* **2020**, *231*, 115916. [CrossRef]
26. Lindgren, T.; Wang, H.; Beermann, N.; Vayssieres, L.; Hagfeldt, A.; Lindquist, S.-E. Aqueous photoelectrochemistry of hematite nanorod array. *Sol. Energy Mater. Sol. Cells* **2002**, *71*, 231–243. [CrossRef]
27. Zhang, D.S.; Downing, J.A.; Knorr, F.J.; McHale, J.L. Nanostructured semiconductor composites for solar cells. *J. Chem. B* **2006**, *110*, 32–36.
28. Ge, M.; Cao, C.; Huang, J.; Li, S.; Lai, Y. A review of one-dimensional TiO_2 nanostructured materials for environmental and energy applications. *J. Mater. Chem. A* **2016**, *4*, 6772–6801. [CrossRef]
29. Shuang, S.; Zheng, X.; Zhang, Z. Review: Nanostructured TiO_2 for enhanced photocatalytic property by glancing angle deposition method. *J. Harbin Inst. Technol.* **2017**, *24*, 1–11.
30. Cheng, X.; Zhang, Y.; Bi, Y. Spatial dual-electric fields for highly enhanced the solar water splitting of TiO_2 nanotube arrays. *Nano Energy* **2019**, *57*, 542–548. [CrossRef]
31. Nazim, M.; Khan, A.A.P.; Asiri, A.M.; Kim, J.H. Exploring rapid photocatalytic degradation of organic pollutants with porous CuO nanosheets: Synthesis, dye removal, and kinetic studies at room temperature. *ACS Omega* **2021**, *6*, 2601–2612. [CrossRef]
32. Cani, D.; Waal, J.C.; Pescarmona, P.P. Highly-accessible, doped TiO_2 nanoparticles embedded at the surface of SiO_2 as photocatalysts for the degradation of pollutants under visible and UV radiation. *Appl. Catal. A Gen.* **2021**, *621*, 118179. [CrossRef]
33. D'Angelo, D.; Filice, S.; Scarangella, A.; Iannazzo, D.; Compagnini, G.; Scalese, S. Bi_2O_3/Nexar® polymer nanocomposite membranes for azo dyes removal by UV–vis or visible light irradiation. *Catal. Today* **2019**, *321–322*, 158–163. [CrossRef]
34. Li, Z.Q.; Chen, X.T.; Xue, Z.L. Bi_2MoO_6 microstructures: Controllable synthesis, growth mechanism, and visible-light-driven photocatalytic activities. *CrystEngComm* **2013**, *15*, 498–508. [CrossRef]

35. Zhang, L.; Xu, T.; Zhao, X.; Zhu, Y. Controllable synthesis of Bi_2MoO_6 and effect of morphology and variation in local structure on photocatalytic activities. *Appl. Catal. B Environ.* **2010**, *98*, 138–146. [CrossRef]
36. Li, N.; Gao, H.; Wang, X.; Zhao, S.; Da, L.; Yang, G.; Gao, X.; Fan, H.; Gao, Y.; Ge, L. Novel indirect Z-scheme g-C3N4/Bi_2MoO_6/Bi hollow microsphere heterojunctions with SPR-promoted visible absorption and highly enhanced photocatalytic performance. *Chin. J. Catal.* **2020**, *41*, 426–434. [CrossRef]
37. Mia, M.S.; Yao, P.; Zhu, X.; Lei, X.; Chen, G. Degradation of textile dyes from aqueous solution using tea-polyphenol/Fe loaded waste silk fabrics as Fenton-like catalysts. *RSC Adv.* **2021**, *11*, 8290–8305. [CrossRef]
38. Li, H.; Zhang, T.; Pan, C.; Pu, C.; Hu, Y.; Hu, X.; Liu, E.; Fan, J. Self-assembled Bi_2MoO_6/TiO_2 nanofiber heterojunction film with enhanced photocatalytic activities. *Appl. Surf. Sci.* **2017**, *391*, 303–310. [CrossRef]
39. Cai, K.; Lv, S.; Song, L.; Chen, L.; He, J.; Chen, P.; Au, C.; Yin, S. Facile preparation of ultrathin Bi_2MoO_6 nanosheets for photocatalytic oxidation of toluene to benzaldehyde under visible light irradiation. *J. Solid State Chem.* **2019**, *269*, 145–150. [CrossRef]
40. Yunarti, R.T.; Safitri, T.N.; Dimonti, L.C.C.; Aulia, G.; Khalil, M.; Ridwan, M. Facile synthesis of composite between titania nanoparticles with highly exposed (001) facet and coconut shell-derived graphene oxide for photodegradation of methylene blue. *J. Phys. Chem. Solids* **2022**, *160*, 110357. [CrossRef]
41. Dinh, C.T.; Yen, H.; Kleitz, F.; Do, T.O. Three-dimensional ordered assembly of thin-shell Au/TiO_2 hollow nanospheres for enhanced visible-light-driven photocatalysis. *Angew. Chem. Int. Ed. Engl.* **2014**, *53*, 6618–6623. [CrossRef]
42. Li, Q.; Li, L.; Long, X.; Tu, Y.; Ling, L.; Gu, J.; Hou, L.; Xu, Y.; Liu, N.; Li, Z. Rational design of MIL-88A(Fe)/Bi_2WO_6 heterojunctions as an efficient photocatalyst for organic pollutant degradation under visible light irradiation. *Opt. Mater.* **2021**, *118*, 111260. [CrossRef]
43. Ali, H.; Guler, A.C.; Masar, M.; Urbanek, P.; Urbanek, M.; Skoda, D.; Suly, P.; Machovsky, M.; Galusek, D.; Kuritka, I. Solid-state synthesis of direct Z-scheme Cu_2O/WO_3 nanocomposites with enhanced visible-light photocatalytic performance. *Catalysts* **2021**, *11*, 293. [CrossRef]
44. Tian, J.; Hao, P.; Wei, N.; Cui, H.; Liu, H. 3D Bi_2MoO_6 nanosheet/TiO_2 nanobelt heterostructure: Enhanced photocatalytic activities and photoelectochemistry performance. *ACS Catal.* **2015**, *5*, 4530–4536. [CrossRef]
45. Yus, J.; Ferrari, B.; Sanchez-Herencia, A.J.; Gonzalez, Z. Understanding the effects of different microstructural contributions in the electrochemical response of Nickel-based semiconductor electrodes with 3D hierarchical networks shapes. *Electrochim. Acta* **2020**, *335*, 135629. [CrossRef]
46. Zhao, K.; Zhao, S.; Gao, C.; Qi, J.; Yin, H.; Wei, D.; Mideksa, M.F.; Wang, X.; Gao, Y.; Tang, Z.; et al. Metallic Cobalt–Carbon Composite as Recyclable and Robust Magnetic Photocatalyst for Efficient CO_2 Reduction. *Small* **2018**, *14*, 1800762. [CrossRef]
47. Singh, S.; Sangle, A.L.; Wu, T.; Khare, N.; Macmanus-Driscoll, J.L. Growth of doped $SrTiO_3$ ferroelectric nanoporous thin films and tuning of photoelectrochemical properties with switchable ferroelectric polarization. *ACS Appl. Mater. Interfaces* **2019**, *11*, 45683–45691. [CrossRef]
48. Jiang, S.; Liu, J.; Zhao, K.; Cui, D.; Liu, P.; Yin, H.; Al-Mamun, M.; Lowe, S.E.; Zhang, W.; Zhong, Y.L.; et al. Ru(bpy)32+-sensitized {001} facets $LiCoO_2$ nanosheets catalyzed CO_2 reduction reaction with 100% carbonaceous products. *Nano Res.* **2021**, *15*, 1061–1068. [CrossRef]
49. Zhou, T.; Zhang, H.; Zhang, X.; Yang, W.; Cao, Y.; Yang, P. BiOI/$Bi_2O_2CO_3$ two-dimensional heteronanostructures with boosting charge carrier separation behavior and enhanced visiblelight photocatalytic performance. *J. Phys. Chem. C* **2020**, *124*, 20294–20308. [CrossRef]
50. Hu, J.R.T.; Gong, Q.; Wang, Q.; Sun, B.; Gao, T.; Cao, P.; Zhou, G. Spherical Bi_2WO_6/Bi_2S_3/MoS_2 n-p heterojunction with excellent visible-light photocatalytic reduction Cr(VI) activity. *Nanomaterials* **2020**, *10*, 1813.